

# 3D Shape Analysis of the Brain Cortex With Application to Autism

M. Nitzken, et al.  
*IEEE, 2011*



**NeuroSpectrum Insights, Inc.**

[info@neurospectruminsights.com](mailto:info@neurospectruminsights.com)

[www.neurospectruminsights.com](http://www.neurospectruminsights.com)

## 3D SHAPE ANALYSIS OF THE BRAIN CORTEX WITH APPLICATION TO AUTISM

M. Nitzken<sup>1</sup>, M. F. Casanova<sup>2</sup>, G. Gimel'farb<sup>3</sup>, F. Khalifa<sup>1</sup>, A. Elnakib<sup>1</sup>, A. E. Switala<sup>2</sup>, and A. El-Baz<sup>1\*</sup>

<sup>1</sup>BioImaging Laboratory, Bioengineering Department, University of Louisville, Louisville, KY, USA.

<sup>2</sup>Department of Psychiatry and Behavioral Sciences University of Louisville, Louisville, KY, USA.

<sup>3</sup>Department of Computer Science, University of Auckland, Auckland, New Zealand.

### ABSTRACT

To discriminate more accurately between autistic and normal brains, we detect the brain cortex variability using a spherical harmonic analysis that represents a 3D surface supported by the unit sphere with a linear combination of special basis functions, called spherical harmonics (SHs). The proposed 3D shape analysis is carried out in five steps: (i) 3D brain cortex segmentation, with a deformable 3D boundary, controlled by two probabilistic visual appearance models (the learned prior and the estimated current appearance one); (ii) 3D Delaunay triangulation to construct a 3D mesh model of the brain cortex surface; (iii) mapping this model to the unit sphere; (iv) computing the SHs for the surface; and (v) determining the number of the SHs to delineate the brain cortex. We describe the brain shape complexity with a new shape index, the estimated number of the SHs, and use it for  $K$ -nearest classification of normal and autistic brains. Initial experiments suggest that our shape index is a promising supplement to the current autism diagnostic techniques.

**Index Terms**— Autism, shape analysis, brain cortex segmentation, spherical harmonics.

### 1. INTRODUCTION

Autistic Spectrum Disorder (ASD) or autism, is a complex neurological disability that is characterized by qualitative abnormalities in behavior and higher cognitive functions. It typically appears during the first three years of life and severely impacts the development of social interaction and communication skills [1]. In 2009 about 0.9% of American children fell into the autistic spectrum [2]. Both children and adults with classic autism encounter difficulties in social interaction, communication, and the use of language, and have limited imagination resulting in restricted, repetitive, and stereotypical behavioral and activity patterns [3].

Conventional autism diagnostics rely on recording patient reactions to varied stimuli through periodic screening interviews. Early observations by parents can greatly reduce the false positive rate and circumvent unnecessary referrals [4]. However, the diagnosis is subject to human observational and perceptual errors because autism has many forms and personality traits that may be difficult to detect. A more objective computer aided diagnosis (CAD) is a prime necessity in this field.

Recent advances in neuro-imaging suggest new non-invasive ways to automate autism detection by revealing differences between quantitative characteristics of normal and autistic brains. Almost 60 years ago, an increased head size was the first observed characteristic in children with autism [5]. Subsequent (including postmortem)

studies have revealed an enlarged head circumference in autistic patients (i.e., macrocephaly defined as the circumference above the 97th percentile, or two standard deviations above the mean [6]), as well as an increase in brain size, volume, and weight. Courchesne et al. [7] showed that children with autism have an ordinary brain size at birth, but between the ages of two and four experience accelerated brain growth, resulting in an increased brain volume relative to a normal brain. By adolescence and adulthood, the differences in the mean brain size between the two groups diminish largely due to the increased relative growth in the control group [6].

In addition to the enlarged brain size, alterations of different brain structures have been found in autistic individuals when compared to normal ones. For example, MRI studies have shown abnormalities in the corpus callosum (CC) of autistic brains. Vidal et al. [8] localized the autism-related thinning of the CC by relating the CC thickness to the distance between uniformly spaced points on the CC surface and the CC medial line (i.e., the average curve between the superior and inferior CC boundaries). El-Baz et al. [9] reported significant differences in all anatomical divisions, i.e. splenium, rostrum, genu and body of autistic CCs by applying a 3D shape analysis of the corpus callosum surface. Another autistic brain abnormality is cortical grey matter enlargement, particularly in the frontal and temporal lobes [10]. Additionally, MRI studies have shown an increased volume in cerebellar white matter (CWM) in young children with autism relative to controls and an abnormal CWM anatomy in autistic brains [6, 7].

Instead of examining the volumetric changes in individual brain structures, our recent diagnosis system [11] quantified differences between the shape of CWM gyrifications for autistic and normal subjects by analyzing 3D MRI brain images and classifies the subjects based on the thickness of CWM gyrification. This paper attempts to analyze and quantify differences between the whole 3D brain cortex shapes for autism and normal subjects in order to discriminate between them more accurately.

### 2. 3D SHAPE ANALYSIS FRAMEWORK

The proposed analysis begins with brain cortex segmentation from 3D MR images, through the use of a deformable 3D boundary that is controlled by two probabilistic visual appearance models (the learned prior and the estimated current appearance one). Then a 3D mesh model of the cortex surface is mapped to a unit sphere, and approximated using a linear combination of spherical harmonics (SHs). The number of SHs yields a desired approximation accuracy that can be used as a new shape index describing the complexity of the brain shape. Then a  $K$ -nearest classifier separates the autistic and normal subjects by their shape indexes.

\* Corresponding Author:- Tel: (502) 852-5092, Fax: (502) 852-6806, E-mail: aselba01@louisville.edu

## 2.1. Brain cortex segmentation

The accurate cortex segmentation from 3D T2-MR images is a challenging problem, because there are no clear differences between intensities in the cortex and surrounding organs. To overcome this problem, we use a conventional 3D parametric deformable boundary [12] but control its evolution with two probabilistic visual appearance models, namely, a learned cortex appearance prior and a current appearance model of the image to be segmented. The prior is a 3D Markov-Gibbs random field (MGRF) model of the cortex intensities with translation- and rotation-invariant pairwise voxel interaction, being learned analytically from training data in accord with [13]. The current appearance is modeled by a mixed marginal distribution of the voxel intensities in both the brain cortex and surrounding tissues. To extract the voxel-wise model of the current cortex appearance, the mixture is precisely approximated with a linear combination of discrete Gaussians (LCDG) [14, 15] and automatically separated into the cortex and background LCDG models. Fig. 1 demonstrates the results of our cortex segmentation. The Gibbs energies for each of the brain cortex voxel are higher than for any other brain tissues, making the proposed approach very accurate (our segmentation error with respect to the radiologist's "ground truth" is about 2.3%). For more details about the segmentation model and for a comparison with other approaches see [16].

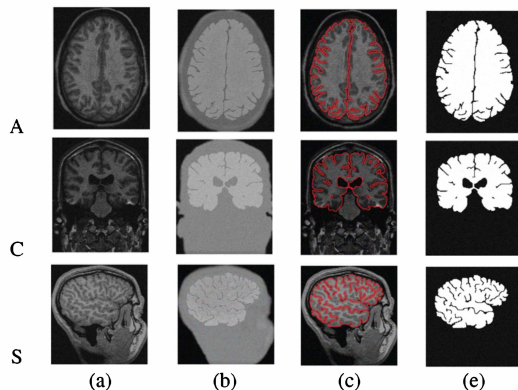


**Fig. 1.** 3D brain cortex segmentation projected onto 2D axial (A), coronal (C), and sagittal (S) planes for visualization: 2D slices of the original T2-MRI images (a), pixel-wise Gibbs energies (b), our segmentation (c), and the radiologist's segmentation (d).

## 2.2. Spherical harmonics (SHs) shape analysis

Spectral SH analysis [17] considers 3D surface data as a linear combination of specific basis functions. In our case, the surface of the segmented brain cortex is approximated first by a triangulated 3D mesh (see Fig. 2) built with an algorithm by Fang and Boas [18]. Secondly, the brain cortex surface for each subject is mapped for the SH decomposition to the unit sphere. We propose a novel mapping approach, called "Attraction-Repulsion" that calls for all the mesh nodes to meet two conditions: (i) the unit distance of each node from the brain cortex center as shown in Fig. 3, and (ii) an equal distance of each node from all of its nearest neighbors as shown in Fig. 4.

To detail our Attraction-Repulsion Algorithm (see its summary in Algorithm 1), let  $\tau$  denote the iteration index,  $I$  be the total number of the mesh nodes (in all the experiments below  $I = 48962$  nodes), and  $\mathbf{P}_{\tau,i}$  be the Cartesian coordinates of the surface node

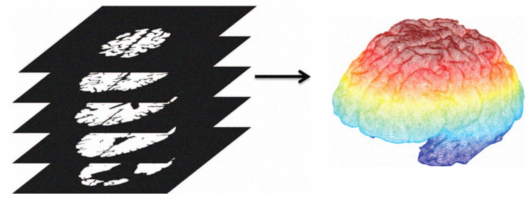


**Fig. 2.** Generating a 3D mesh for the brain cortex surface from a stack of successive segmented 2D T2-MR slices.

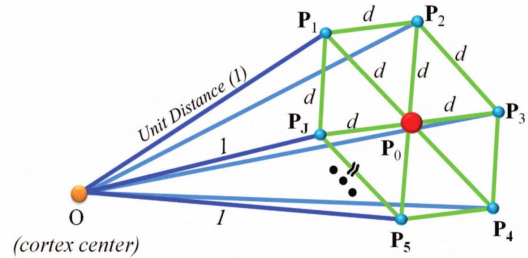


**Fig. 3.** 3D illustration of the unit distance from all surface nodes to the center of the brain cortex.

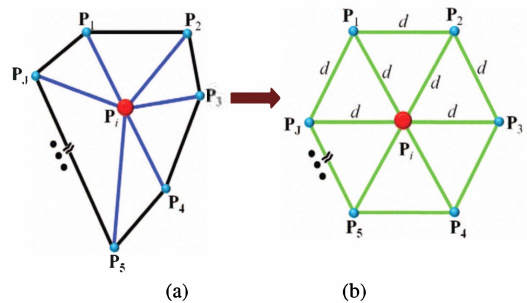


**Fig. 4.** 2D illustration of the neighbors rearrangement: initial (a) vs. final equidistant locations (b) in all the directions.

$i$  at iteration  $\tau$ ;  $i = 1, \dots, I$ . Let  $J$  be the number of the neighbors for a mesh node (see e.g., Fig. 4) and  $d_{\tau,ij}$  denote the Euclidean distance between the surface nodes  $i$  and  $j$  at iteration  $\tau$  (as shown in Fig. 4(b)), where  $i = 1, \dots, I$  and  $j = 1, \dots, J$ . Let  $\Delta_{\tau,ji} = \mathbf{P}_{\tau,j} - \mathbf{P}_{\tau,i}$  denote the displacement between the nodes  $j$  and  $i$  at iteration  $\tau$ . Let  $C_{A,1}, C_{A,2}, C_R$  be the attraction and repulsion constants, respectively, that control the displacement of each surface node.

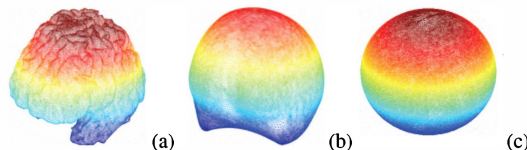


**Fig. 5.** Brain cortex mesh (a), its smoothed version (b), and the Attraction-Repulsion mapping to the unit sphere (c).

The starting attraction step of the proposed mapping tends to center each node  $\mathbf{P}_i$ ;  $i = 1, \dots, I$ , with respect to its neighbors by

---

**Algorithm 1: Attraction-Repulsion Algorithm**


---

**Initialization**

- Construct the 3D brain cortex mesh (Fig. 5.a).
- Smooth it by the Laplacian filtering (Fig. 5.b).
- Initialize the mapping of the smoothed mesh to the unit sphere.

**Repeat**

- **For**  $i = 1 \rightarrow I$ 
  - **Attraction:**
    - \* Select a node to process.
    - \* Update the node using Eq. (1)
  - **Repulsion:**
    - \* Update the node using Eq. (2).
- **End** (all nodes in the mesh are shifted and back-projected onto the unit sphere).

---

**While** changes in the node positions occur (Fig. 5.c).

---

adjusting iteratively its location:

$$\mathbf{P}'_{\tau,i} = \mathbf{P}_{\tau,i} + C_{A,1} \sum_{j=1;j \neq i}^J \Delta_{\tau,j,i} d_{\tau,j,i}^2 + C_{A,2} \frac{\Delta_{\tau,j,i}}{d_{\tau,j,i}} \quad (1)$$

where the factor  $C_{A,2}$  keeps the tightly packed nodes from collision and also pushes the adjusted nodes away from their neighbors if a certain neighbor is much closer than the others.

The subsequent repulsion step inflates the whole mesh by pushing all the nodes outwards to become evenly spaced after their final back-projection onto the unit sphere along the rays from the center of the sphere. To ensure the nodes that have not been shifted will not collide with the altered node, the location of each node  $\mathbf{P}_i$ ;  $i = 1, \dots, I$ , is updated before the back-projection as follows:

$$\mathbf{P}^o_{\tau+1,i} = \mathbf{P}'_{\tau,i} + \frac{C_R}{2I} \sum_{j=1;j \neq i}^I \left( \frac{\Delta_{\tau,j,i}}{|\Delta_{\tau,j,i}|^2} \right) \quad (2)$$

where a repulsion constant  $C_R$  controls the displacement of each surface node and establishes a balance between the processing time and accuracy (e.g., a smaller  $C_R$  values guarantees that the node faces will not become crossed during the iterations at the expense of the increased processing time). All the experiments below are obtained with  $0.3 \leq C_R \leq 0.7$ .

The original brain cortex, mapped to the unit sphere with the proposed Attraction-Repulsion algorithm, is approximated by a linear combination of SHs, the lower-order harmonics being sufficient to represent more generic information, while the finer details requiring the higher-order ones. The SHs are generated by solving an isotropic heat equation for the cortex surface on the unit sphere. Let  $\mathcal{S} : \mathbf{M} \rightarrow \mathbf{U}$  denote the mapping of a cortical mesh  $\mathbf{M}$  to the unit sphere  $\mathbf{U}$ . Each node  $\mathbf{P} = (x, y, z) \in \mathbf{M}$  mapped to the spherical position  $\mathbf{u} = S(\mathbf{P})$  is represented by the spherical coordinates  $\mathbf{u} = (\sin \theta \cos \varphi, \sin \theta \sin \varphi, \cos \theta)$  where  $\theta \in [0, \pi]$  and  $\varphi \in [0, 2\pi)$  are the polar and azimuth angles, respectively. The SH  $Y_{\alpha\beta}$  of degree  $\alpha$  and order  $\beta$  is defined as [19]:

$$Y_{\alpha\beta} = \begin{cases} c_{\alpha\beta} G_{\alpha}^{|\beta|} \cos \theta \sin(|\beta|\varphi) & -\alpha \leq \beta \leq -1 \\ \frac{c_{\alpha\beta}}{\sqrt{2}} G_{\alpha}^{|\beta|} \cos \theta & \beta = 0 \\ c_{\alpha\beta} G_{\alpha}^{|\beta|} \cos \theta \cos(|\beta|\varphi) & 1 \leq \beta \leq \alpha \end{cases} \quad (3)$$

where  $c_{\alpha\beta} = \left( \frac{2\alpha+1}{2\pi} \frac{(\alpha-|\beta|)!}{(\alpha+|\beta|)!} \right)^{\frac{1}{2}}$  and  $G_{\alpha}^{|\beta|}$  is the associated Legendre polynomial of degree  $\alpha$  and order  $\beta$ . For the fixed  $\alpha$ , the polynomials  $G_{\alpha}^{\beta}$  are orthogonal over the range  $[-1, 1]$ . As shown in [19], the Legendre polynomials are effective in calculating SHs, and this is the main motivation behind their use in this work.

Finally, the brain cortex is reconstructed from the SHs of Eq. (3). In the case of the SHs expansion, the standard least-square fitting does not model accurately the 3D shape of the brain cortex and can miss some of the shape details that discriminate between the autistic and normal brains. To circumvent this problem, we used the iterative residual fitting by Shen et al. [20] that accurately approximates 3D gyrifications of an autistic and normal brain cortex. As demonstrated in Fig. 6, the model accuracy does not significantly change for the control subject from the 25 to 60 SHs, while it continues to increase for the autistic subject.

### 2.3. Quantitative brain cortex shape analysis

Our main hypothesis is that the brain cortex gyral frequency for autistic subjects is greater than for control ones as in Fig. 6, so that more SHs have to be used for an accurate approximation of the brain cortex gyrifications. Therefore, the number of the SHs, after which there is no significant changes in the approximations, can be used as a new shape index quantifying the cortex complexity of both the autistic and normal brains. Due to the unit sphere mapping, the original brain cortex mesh for each subject is inherently aligned with the mesh for the approximate shape, and the sum of the Euclidean distances between the corresponding nodes gives the total error between both the mesh models. As shown in Fig. 7, the total error curves for the increasing number  $\mathcal{K}$  of the SHs can be used as a discriminatory feature to differentiate between the subjects.

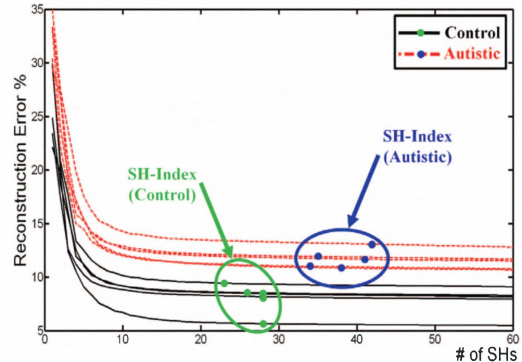


**Fig. 7.** Estimation of the shape index from the total cortex approximation error for autistic and normal subjects.

### 3. EXPERIMENTAL RESULTS AND CONCLUSIONS

The proposed approach has been tested on *in-vivo* data that has been collected from 45 subjects (15 autistic subjects of age  $22.1 \pm 9.7$  years and 30 control subjects of age  $20.7 \pm 8.5$  years). The subjects were scanned using a 1.5 Tesla GE MRI system with voxel resolution of  $0.9375 \times 0.9375 \times 1.5 \text{ mm}^3$  using a T2 weighted imaging sequence protocol. The “ground truth” diagnosis to evaluate the classification accuracy for each patient was given by five medical experts.



	Original mesh	1 SH	15 SHs	25 SHs	40 SHs	50 SHs	60 SHs
C							
A							

**Fig. 6.** Approximation of the 3D brain cortex shape for autistic (A) and normal subjects (C).

The training subset for classification (10 persons in Fig. 7) was arbitrarily selected among all the 45 subjects. The classification accuracy of the  $k$ -nearest classifier for both the training and test subjects was evaluated using the  $\chi^2$ -test at the 95% confidence level: this correctly classified 14 out of 15 autistic subjects (93.3% accuracy), and 30 out of 30 control subjects (100% accuracy). The accuracy of the traditional volumetric approach is 8 out of 15 autistic subjects (53.3%), and 19 out of 30 control subjects (63.3%) at the 95% confidence level. These results highlight the advantage of the proposed diagnostic tool.

In total, these preliminary results show that the 3D brain cortex shape analysis is able to accurately discriminate between autistic and normal subjects. Our proposal substantially differs from known diagnostic techniques that exploit only volumetric descriptions of different brain structures and thus are in principle more sensitive to the selection of ages and segmentation errors [6]. In contrast, we derive the efficient quantitative classification feature from the whole 3D cortex shape. Our experiments demonstrate that the proposed general geometric feature of cortex gyrifications has statistically significant differences for the 45 normal and autistic subjects under consideration. In the future, we will investigate different brain structures in order to quantitatively characterize their temporal development and changes in an autistic brain. To validate and possibly modify the proposed approach, we will test it on larger data sets with a known ground truth (i.e., the doctors' diagnosis).

#### 4. REFERENCES

- [1] P. Brambilla, A. Hardan, S. U. di Nemi, et al., "Brain anatomy and development in autism: review of MRI studies," *Brain Research Bulletin*, vol. 61, pp. 557–569, 2003.
- [2] A. Park, "Autism numbers are rising. The question is why?," *Time*, Dec. 19th 2009, [on-line; accessed on Jan 27th 2011], <http://www.time.com/time/health/article/0,8599,1948842,00.html>.
- [3] N. J. Minshew and J. B. Payton, "New perspectives in autism, Part I: The clinical spectrum of autism," *Curr. Probl. Pediatr.*, vol. 18, no. 10, pp. 561–610, 1988.
- [4] D. L. Robins, D. Fein, M. L. Barton, and J. A. Green, "The modified checklist for autism in toddlers: an initial study investigating the early detection of autism and pervasive developmental disorders," *J. Autism Dev. Disord.*, vol. 31, no. 2, pp. 131–144, 2001.
- [5] L. Kanner, "Autistic disturbances of affective contact," *Nervous Child*, vol. 2, pp. 217–250, 1943.
- [6] E. Aylward, N. J. Minshew, K. Field, et al., "Effects of age on brain volume and head circumference in autism," *Neurology*, vol. 59, no. 2, pp. 175–183, 2002.
- [7] E. Courchesne, R. Carper, and N. Akshoomoff, "Evidence of brain overgrowth in the first year of life in autism," *J. Amer. Med. Assoc.*, vol. 290, pp. 337–344, 2003.
- [8] C. N. Vidal, R. Nicolson, T. J. DeVito, et al., "Mapping corpus callosum deficits in autism: an index of aberrant cortical connectivity," *Biol. Psychiatry*, vol. 60, pp. 218–225, 2006.
- [9] A. El-Baz, A. Elnakib, M. F. Casanova, G. Gimelfarb, et al., "Accurate Automated Detection of Autism Related Corpus Callosum Abnormalities," *International Journal of Medical Systems (JMS)*, 2011 (in press).
- [10] R. A. Carper, P. Moses, Z. D. Tigue, and E. Courchesne, "Cerebral lobes in autism: early hyperplasia and abnormal age effects," *Neuroimage*, vol. 16, no. 4, pp. 1038–1051, 2002.
- [11] A. El-Baz, M. F. Casanova, G. Gimelfarb, et al., "Autism diagnostics by 3D texture analysis of cerebral white matter gyrifications," *Proc. of International Conference on Medical Image Computing and Computer-Assisted Intervention (MICCAI'07), Brisbane, Australia, 2007*, vol. 2, pp. 882–890, 2007.
- [12] M. Kass, A. Witkin, and D. Terzopoulos, "Snakes: Active contour models," *Int. J. of Computer Vision*, pp. 321–331, 1987.
- [13] G. Gimelfarb, *Image Textures and Gibbs Random Fields*, Kluwer Academic, 1999.
- [14] A. Farag, A. El-Baz, and G. Gimelfarb, "Precise segmentation of multimodal images," *IEEE Trans. on Image Processing*, vol. 15, no. 4, pp. 952–968, 2006.
- [15] A. El-Baz and G. Gimelfarb, "EM Based Approximation of Empirical Distributions with Linear Combinations of Discrete Gaussians," in: *Proc. IEEE Int. Conf. on Image Processing (ICIP'07), San Antonio, Texas, USA, Sept. 16–19, 2007*, vol. IV, pp. 373–376, 2007.
- [16] A. El-Baz, M. Casanova, et al., "Dyslexia diagnostics by 3D texture analysis of cerebral white matter gyrifications," in *ICPR'08, Tampa, FL, USA Dec. 8–11, 2008*, 1–4.
- [17] M. K. Chung, L. Shen, K. M. Dalton, et al., "Weighted Fourier series representation and its application to quantifying the amount of gray matter," *IEEE Trans. on Med. Imaging*, vol. 26, pp. 566–581, 2007.
- [18] Q. Fang and D. Boas, "Tetrahedral mesh generation from volumetric binary and gray-scale images," in: *ISBI'09, June 28 – July 1, 2009, Boston, MA, USA*, pp. 1142–1145, 2009.
- [19] R. Courant and D. Hilbert, *Methods of Mathematical Physics*, Vol. II. Interscience, New York, 1953.
- [20] L. Shen and M. K. Chung, "Large-scale modeling of parametric surfaces using spherical harmonics," in *Proc. 3<sup>rd</sup> Int. Symp. 3DPVT, Chapel Hill, NC, USA June 14–16, 2006*, IEEE, pp. 294–301, 2006.